International Journal of Thermal Sciences 134 (2018) 453–464

Contents lists available at ScienceDirect

International Journal of Thermal Sciences

journal homepage: www.elsevier.com/locate/ijts

Effect of vortex promoter shape on heat transfer in MHD duct flow with axial magnetic field

Wisam K. Hussam[a,b,*], Ahmad H.A. Hamid[c], Zhi Y. Ng[b], Gregory J. Sheard[b]

[a] School of Engineering, Australian College of Kuwait, Safat, Kuwait
[b] The Sheard Lab, Department of Mechanical and Aerospace Engineering, Monash University, VIC, 3800, Australia
[c] Faculty of Mechanical Engineering, Universiti Teknologi MARA, 40450, Selangor, Malaysia

ARTICLE INFO

Keywords:
Magnetohydrodynamics
Channel flow
Triangular cylinder
Quasi-two-dimensional model
Heat transfer

ABSTRACT

The heat transfer from the side-wall of a duct through which an electrically conducting fluid flows within a strong transverse magnetic field is numerically investigated using high-resolution numerical simulation. Parameter ranges considered are $0 \leq Ha \leq 2400$ and $100 \leq Re \leq 3000$ for a constant blockage ratio of 1/4. The gain in the heat transfer using obstacles of different geometric shapes are compared. For $Ha = 320$, a maximum heat transfer enhancement of 78% is obtained when using the square cylinder at a modes $Re = 1000$, while the triangular cylinder outperformed the various other vortex promoter geometries at $Re = 2000$ yielding a 75% improvement.. However, at a higher Hartmann number of $Ha = 2400$, a maximum heat transfer augmentation of 16% and 40% is obtained for the triangular cylinder at $Re = 1000$ and 2000, respectively. This suggests that for a duct flow under the influence of a strong magnetic field, the triangular obstacle is a superior heat transfer promoter geometry compared to the square or circular cylinders. A further net power analysis reveals that the heat transfer enhancement dominates over the pumping power to produce net benefits for even a modest heat transfer enhancement.

1. Introduction

Magnetohydrodynamic (MHD) flow in rectangular ducts under an imposed magnetic field occurs in metallurgical processing applications as well as within cooling blankets and tritium breeder modules proposed for future magnetic confinement fusion reactors [1]. Liquid metal blankets in fusion reactors need to be able to reliably carry heat away from the fusion reaction. The economic premium in decreasing the size of magnetic coils in fusion reactors can be achieved as a result of enhancing heat transfer efficiency of fusion reactor blankets which is highlighted by Khan and Davidson [2].

The electrically conducting fluid that circulates within the blanket is exposed to a sufficiently strong magnetic field to confine the plasma. The Lorentz force arising from the interaction of the fluid with the high magnetic field has a significant effect on the velocity distribution and the turbulence intensity, and exerts a braking force on the flow [3]. Therefore, magnetohydrodynamic duct flows can be characterised by laminar flow structures as velocity fluctuations in the direction of the magnetic field are suppressed while vortices elongate and align with the magnetic field [4–6]. Under these conditions, MHD duct flows comprise a two-dimensional core flow separated by boundary layers on the duct walls. The duct walls perpendicular to the magnetic field form boundary layers known as Hartmann layers, which exert a friction on the interior two-dimensional flow. This inspired the development of quasi-two-dimensional models for these flows. For fusion reactor cooling blankets, the suppression of these turbulent structures is detrimental to the operational efficiency, where given the large amounts of heat that must be removed. The heat transfer can be enhanced by promoting turbulence near the heated wall using obstacles placed inside the duct, where an increasing body of evidence is demonstrating that the heat transport characteristics around the obstacle depend strongly on the shape of the obstacle [7–10]. The disturbances resulting from these promoters induce a significant velocity component in the direction perpendicular to the magnetic field that promotes mixing and thereby improves convective heat transport in this direction.

In addition to liquid metal cooling systems in fusion reactors, other liquid metal duct flow applications include the cooling of nuclear fission reactors and high-performance computing infrastructure. Beyond MHD applications, channel flows exhibiting quasi-two-dimensional characteristics appear in applications ranging from microfluidics through to geophysical flows.

In the present study, the efficacy of a triangular cylinder aligned

* Corresponding author. Department of Mechanical and Aerospace Engineering, Monash University, VIC, 3800, Australia.
E-mail addresses: w.alsaadi@ack.edu.kw, wisam.alsaadi@monash.edu (W.K. Hussam).

https://doi.org/10.1016/j.ijthermalsci.2018.06.012
Received 5 July 2017; Received in revised form 11 April 2018; Accepted 8 June 2018

Nomenclature

a	duct depth (out-of-plane)
A	instability mode amplitude
B	magnetic field
C_d	cylinder drag coefficient
C_l	cylinder lift coefficient
C_p	constant pressure specific heat capacity
d	side length of triangular cylinder
E_c	Eckert number
f	wake oscillation frequency
$F_d^{'}$	drag force per unit span
$F_l^{'}$	lift force per unit span
h	duct height
H	Hartmann friction parameter
Ha	Hartmann number
L_{duct}	duct length
$\mathcal{L}^2$	integral of velocity magnitude throughout the domain
n	number of Hartmann layers
N	interaction parameter
N_{el}	number of spectral elements in mesh
$\overline{Nu}$	time-averaged Nusselt number
$\overline{Nu_0}$	time-averaged Nusselt number in empty channel
Nu_w	instantaneous local Nusselt number
p	pressure
Δp	pressure drop across channel
Δp_0	pressure drop across channel with no cylinder
ΔP_{net}	overall net power enhancement
P_{heat}	heating power
P_{flow}	pumping power
Pe	Péclet number
Pr	Prandtl number
Re	Reynolds number
Re_c	critical Reynolds number
Re_m	magnetic Reynolds number
St	Strouhal number
t	time
u	streamwise component of velocity
$\mathbf{u}$	velocity vector field
U	peak inlet velocity
x	Cartesian coordinate in flow direction
x_u	length to upstream boundary
x_d	length to downstram boundary
y	Cartesian coordinate across channel

Greek symbols

α	duct aspect ratio
β	blockage ratio
δ_H	Hartmann boundary layer thickness
δ_S	Shercliff boundary layer thickness
$\Delta\theta$	temperature difference between channel side walls
θ	temperature field
θ_f	bulk fluid temperature
θ_0	temperature of fluid entering channel
θ_w	temperature of hot channel side-wall
ζ	mode phase in the Landau equation
ν	kinematic viscosity
ρ	fluid density
σ	linear growth rate in the Landau equation
σ_e	electrical conductivity
Ω	vorticity in x–y plane
ω	angular frequency

with the magnetic field is used to induce disturbances near the heated wall. The rapid suppression of flow disturbances even in the quasi-two-dimensional plane at high Hartmann numbers compels the selection of an obstacle shape that is highly effective at generating shed vortices in a wake that encourages interaction with the hot duct side-wall. Recent hydrodynamic studies of the flow past triangular prisms have demonstrated that vortex shedding initiates at a smaller Reynolds number than the canonical circular cylinder, while the inclined faces and separation from the sharp triangular prism edges can invoke a wider wake [11].

In contrast to the non-MHD flow past circular and square cylinders, the flow and heat transfer past a triangular obstacle have received less attention. For instance, the flow and heat transfer across a triangular cylinder were only investigated in unbounded and bounded configurations by Refs. [12–16] and [17–20], respectively. Abbassi et al. [19] investigated the structure of laminar flow and heat transfer in a differentially heated horizontal channel with a built-in triangular cylinder for Reynolds numbers ranging from $20 \leq Re \leq 250$ for a blockage ratio of 25% and $Pr = 0.71$. The maximum heat transfer enhancement was approximately 85%. Abbassi et al. [21] studied the mixed convection of air in a plane channel heated from below with a built-in triangular prism for Grashof numbers up to 1.5×10^4, at a blockage ratio $\beta = 0.25$ and $Re = 100$. Their results showed that the effect of thermal buoyancy lead to a slight increase in the frequency of vortex shedding and also that the presence of the triangular prism results in a 44% increase in the time-averaged Nusselt number. In another study by Abbassi et al. [22], mixed convection was analysed for a differentially heated two dimensional plane channel with a built-in triangular cylinder. The numerical results demonstrated that for $50 \leq Re \leq 200$ and Grashof number $Gr = 0$, the local and time-averaged Nusselt number can be described by a linear function of $\ln(Re)$. The laminar forced convection fluid flow and heat transfer from a triangular cylinder placed in a channel was investigated numerically by De and Dalal [18] for the Reynolds number range $80 \leq Re \leq 200$ and blockage ratio range $1/12 \leq \beta \leq 1/3$. A criss-cross motion of the vorticity layers was observed at $\beta = 1/3$, whereas they remain in their own half-plane for other cases. The St–Re curve has a flat maximum around $Re = 130$ for $\beta = 1/6$ whereas St increases monotonically with Re for $\beta \geq 1/6$ and with β for $Re > 130$. The local Nusselt number varies with time only in the rear-end of the cylinder due to the vortex shedding, whereas in other two faces it remains unchanged. Srikanth et al. [20] examined the flow and heat transfer across a long triangular cylinder placed in a horizontal channel for Reynolds number range $1 \leq Re \leq 80$ and $Pr = 0.71$ for a fixed blockage ratio of 0.25. Their results found that the average Nusselt number increases with increasing Reynolds number, and that the maximum change between the values of the average Nusselt number for triangular and square obstacles was about 25% for $Re = 1$ and 12.5–15% for $5 \leq Re \leq 45$. More recently, the flow and heat transfer characteristics in a plane channel with a built-in bluff body were investigated numerically by Bouhalleb and Abbassi [23] for $50 \leq Re \leq 250$, gap ratio $0 \leq G \leq 3$ and $\beta = 0.25$ at $Pr = 0.7$. Two body geometries were tested: a triangular prism (TR) and a square cylinder (SQ). Their results showed that maximum heat transfer is achieved when the obstacle is placed at approximately the mid-height of the channel. At $Re = 200$, the maximum heat transfer enhancement was approximately 23% and 32% for the SQ and the TR, respectively, when compared to the empty channel.

Just as the number of studies on the vortex dynamics in a straight channel under a strong magnetic field are limited, the studies pertaining to heat transfer enhancement in a straight channel under these conditions are scarce. An exhaustive literature review yields experimental investigations by Kit et al. [24,25], Kolesnikov and Tsinober [26], Andreev and Kolesnikov [27,28], Frank et al. [29], and numerical

studies by Muck et al. [7], Ueno et al. [30], Dousset and Pothérat [8], Hussam et al. [9,31,32], Hussam and Sheard [33], Chatterjee and Gupta [10], Cassells et al. [34], Hamid et al. [35]. The heat transfer characteristics in a duct with a circular cylinder under a strong axial magnetic field was investigated by Barleon et al. [36], Hussam et al. [9,32], Hussam and Sheard [33], while the case of square cylinder has been investigated recently by Chatterjee and Gupta [10], Cassells et al. [34]. To the best our knowledge, a triangular cylinder with its axis aligned with an imposed magnetic field has not been considered in this configuration. Accordingly, we study numerically the magnetohydrodynamic flow and heat transfer characteristics in a duct with a triangular cylinder subjected to a strong axial magnetic field. The study aims to understand the difference in the MHD flow dynamics and heat transfer characteristics relative to square and circular cylinders under similar flow conditions.

The paper is organised as follows. The problem is defined in Section 2, which also presents the governing equations and parameters. The methodology is presented in Section 3, which describes the numerical method, model setup, boundary conditions and validation. Results and discussion follow in Section 4, with conclusions drawn in Section 6.

2. Problem definition and mathematical formulation

The system of interest is shown schematically in Fig. 1. It consists of a duct carrying an electrically conducting, incompressible fluid confining an equilateral triangular cylinder. The cylinder is placed at the centre of the duct, parallel to the imposed magnetic field vector and perpendicular to the oncoming. The duct has a uniform square cross-section with aspect ratio $\alpha = h/a = 1$, where h is the width and a is height in the magnetic field (out-of-plane) direction. The blockage ratio $\beta = d/h$ characterises the occlusion of the duct by the cylinder, where d is the side length of the triangular cylinder, and throughout this study $\beta = 0.25$. The duct walls and the cylinder are assumed to be electrically insulated, and a homogeneous magnetic field of strength B is imposed parallel to the cylinder axis. The bottom wall of the duct is maintained at a constant wall temperature θ_w, while the top wall and the obstacle are thermally insulated. The strength of the induced field is characterised by the magnetic Reynolds number Re_m, which represents the ratio between the induced and the applied magnetic field. In the present context, the magnetic Reynolds number $Re_m = 1$ and hence the magnetic field induced by the flow is negligible compared to the externally applied field, i.e. the effect of velocity on the magnetic field is negligible [4,5]. Thus the total magnetic field is effectively equal to the applied magnetic field acting in the z-direction only.

Under these conditions the flow is quasi two-dimensional and consists of a core region where the velocity remains unchanged along the magnetic field direction, and a thin Hartmann layer along walls perpendicular to the magnetic field. The quasi-two-dimensional model, hereafter referred to as the SM82 model, has been derived by averaging the flow quantities in the magnetic field direction. The SM82 model neglects the inertial effects within the Hartmann layers, and is accurate to the order $O(Ha^{-1}, N^{-1})$, where $N = \sigma_e B^2 a/\rho U$ is the interaction parameter, $Ha = Ba\sqrt{\sigma_e/\rho\nu}$ is the Hartmann number, σ_e, ν and ρ are the electrical conductivity, kinematic viscosity and density of the liquid metal, respectively, U is the peak inlet velocity, and B is the imposed magnetic field. A thorough description of the SM82 model is given in Refs. [5,6].

Following, for example, Refs. [4,5,34,35] we note that quasi-two-dimensionality is achieved when the time-scale for the Lorentz force to diffuse momentum of a structure size $l_\perp$ along magnetic field lines over length $l_\parallel$, $\tau_{2D} = (\rho/\sigma_e B^2) l_\parallel^2/l_\perp^2$, is shorter than the timescales for viscous diffusion in the perpendicular and parallel planes ($\tau_\nu^\perp = l_\perp^2/\nu$ and $\tau_\nu^\parallel = l_\parallel^2/\nu$, respectively), and the inertial timescale $\tau_u = l_\perp/U$. Taking $l_\parallel = a$, these three conditions can be used respectively to obtain limiting length scales under the model, $l_\perp/a > Ha^{-1/2}$, $l_\perp/a > Ha^{-1}$ and $l_\perp/a > N^{-1/3}$. The second condition is always satisfied under the first condition for $Ha > 1$ [37]. Here lengths are scaled by the side length of the triangular cylinder d, pressure by ρU^2, time by d/U, velocities by U, and temperature by the imposed temperature difference between the bottom and top walls, $\Delta\theta$ [9,38].

2.1. Governing equations and parameters

In this case the non-dimensional magnetohydrodynamic equations of continuity, momentum, and energy reduce to

$$\nabla\cdot\mathbf{u} = 0, \tag{1}$$

$$\frac{\partial\mathbf{u}}{\partial t} + (\mathbf{u}\cdot\nabla)\mathbf{u} = -\nabla p + \frac{1}{Re}(\nabla^2\mathbf{u} - H\mathbf{u}), \tag{2}$$

$$\frac{\partial\theta}{\partial t} + (\mathbf{u}\cdot\nabla)\theta = \frac{1}{Pe}\nabla^2\theta + \frac{E_c}{Re}(\nabla\mathbf{u})^2 + \frac{HaE_c}{4Re}\mathbf{u}^2, \tag{3}$$

where $H = n(d/a)^2 Ha$ is the Hartmann friction parameter which represents the effects of the Lorentz force on the flow, and n is the number of Hartmann layers formed on the duct walls ($n = 2$ in the present configuration). The second and last terms on the right-hand side of equation (3) describe the effects of viscous dissipation and Joule heating, respectively.

In the above equations, the dimensionless Reynolds number, Péclet number and Eckert number parameters are defined as

$$Re = \frac{Ud}{\nu}, \tag{4}$$

$$Pe = Re\,Pr, \tag{5}$$

$$E_c = \frac{U^2}{C_p\delta\theta}. \tag{6}$$

The Prandtl number $Pr = \nu/\kappa_T$, where κ_T is the thermal diffusivity of the fluid.

The heat due to the viscous and Joule dissipation is assumed to be negligible. This is possible when the interaction parameter is large and the flow reaches a quasi-two-dimensional state [5]. It has been reported previously by Hussam et al. [9] that in the context of MHD flow for fusion blanket applications, the contributions of these term are up to seven orders of magnitude smaller than the other terms in equation (3). Furthermore, liquid metals have very high electrical conductivity ($\sigma = O(10^6)\ \Omega^{-1}m^{-1}$; Lyon, 1952), thus Joule dissipation plays a lesser role in the damping of the vortical structures [7,38]. Equation (3) then reduces to

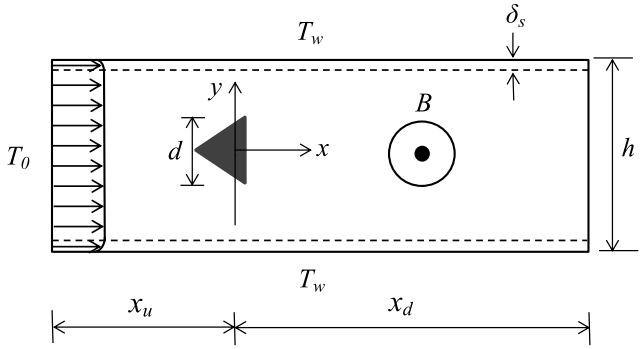

Fig. 1. Schematic representation of the system under investigation. Here the channel is depicted with the triangular obstacle, which is replaced with either a circular or square obstacle as required in the present study. The magnetic field B acts in the out-of-plane direction, parallel to the cylinder axis, δ_S is the thickness of the Shercliff layer, and h and d are the duct height and side lengths of the equilateral triangular cylinder, respectively. The upstream and downstream lengths are x_u and x_d, respectively.

$$\frac{\partial\theta}{\partial t} + (\mathbf{u}\cdot\nabla)\theta = \frac{1}{Pe}\nabla^2\theta. \tag{7}$$

Justification for the omission of the viscous and Joule heating terms is supported by an order of magnitude analysis. Taking

$\rho = 6.3632\ \mathrm{kg/m^3}$,
$\sigma = 3.30737 \times 10^6\ \Omega^{-1}\mathrm{m}^{-1}$,
$\nu = 3.4809 \times 10^{-7}\ \mathrm{m^2/s}$,
$C_p = 188\ \mathrm{J/kg.\ K}$,
$Pr = 0.022$,
$\delta\theta = 250\ \mathrm{K}$,
$U = 0.015\mathrm{m/s}$,
$E_c = 3.191 \times 10^{-7}$

(these values are relevant to the fusion blanket application [39,40]), the viscous dissipation and Joule heating prefactors are as follows: For $Re = 100$ and 3000, $E_c/Re = 3.191 \times 10^{-9}$ and 1.063×10^{-10}, respectively. At $Re = 100$, for $Ha = 320$ and 2400, the Joule dissipation prefactor $HaE_c/4Re = 2.5528 \times 10^{-7}$ and 1.9146×10^{-6}, respectively. At $Re = 3000$, for $Ha = 320$ and 2400, the Joule dissipation prefactor $HaE_c/4Re = 8.5 \times 10^{-9}$ and 6.382×10^{-8}, respectively. By contrast, the thermal diffusion prefactor at $Re = 100$ and 3000 is $1/Pe = 4.5 \times 10^{-1}$ and 1.5×10^{-2}, respectively. Therefore the contributions of the viscous and Joule heating terms are at least five orders of magnitude smaller than the thermal diffusion term.

The total drag coefficient is defined based on the drag force per unit span (F'_d) on the cylinderas

$$C_d = \frac{F'_d}{\frac{1}{2}\rho U^2 d}, \tag{8}$$

and the total lift coefficient is defined based on the lift force per unit span (F'_l) on the cylinderas

$$C_l = \frac{F'_l}{\frac{1}{2}\rho U^2 d}. \tag{9}$$

The wake oscillation frequency f is parameterised by the Strouhal number

$$St = \frac{fd}{U}. \tag{10}$$

The local Nusselt number along the heated side-wall of the channel is defined as

$$Nu_w(x,\ t) = \frac{d}{(\theta_f - \theta_w)}\frac{\partial\theta}{\partial y}\bigg|_{\mathrm{wall}}, \tag{11}$$

where the bulk fluid temperature t_f is calculated using the streamwise velocity component u and the temperature distribution as

$$\theta_f(x,\ t) = \frac{\int_{-h/2}^{h/2} u\theta\ \mathrm{d}y}{\int_{-h/2}^{h/2} u\ \mathrm{d}y}. \tag{12}$$

The time-averaged Nusselt number for heat transfer through the heated wall of the channel is calculated by first taking the time-average of the local Nusselt number ($\overline{Nu}_w(x)$) at each x-station, and then integrating over the length of the heated bottom wall, $L_{\mathrm{duct}} = x_u + x_d$, using

$$\overline{Nu} = \frac{1}{L_{\mathrm{duct}}}\int_{-x_u}^{x_d} \overline{Nu}_w(x)\ \mathrm{d}x. \tag{13}$$

To characterise the effect on the heat transfer due to the addition of a cylinder to the channel, the overall increment of heat transfer is defined as

$$HI = \frac{\overline{Nu} - \overline{Nu_0}}{\overline{Nu_0}}, \tag{14}$$

where $\overline{Nu_0}$ is the time-averaged Nusselt number of the heated region of the duct without the cylinder.

The flow and heat transfer characteristics are investigated for the quasi-two-dimensional channel flow for $100 \le Re \le 3000$, $0 \le Ha \le 2400$, and $\beta = 0.25$. A Prandtl number $Pr = 0.022$ is used throughout this study as it is a representative of the eutectic alloy GaInSn.

All variables are expressed in their dimensionless form hereafter.

3. Numerical procedure

3.1. Spectral-element solver, computational model, and boundary conditions

A nodal spectral-element method is used to discretise the governing flow and energy equations in space, and a third-order scheme based on backwards differentiation is employed for time integration [41]. The boundary conditions imposed on Eqs. (1)–(3) may be written as follows: A no-slip for velocity is imposed on all solid walls. At the inlet ($x = x_u$), the analytical solution to Eqs. (1) and (2) for fully developed quasi-two-dimensional flow through the channel without an obstacle was derived by Refs. [8,37] and is given as

$$u(-x_u,\ y) = \left[\frac{\cosh(\sqrt{H}) - \cosh(2\sqrt{H}\ \beta y)}{\cosh(\sqrt{H}) - 1}\right]. \tag{15}$$

At the outlet ($x = x_d$), a constant reference pressure and a zero normal velocity gradient are imposed. A high order Neumann boundary condition is also applied on the pressure field at the other boundaries to maintain the third-order time accuracy [41]. The temperature of the incoming stream is specified as θ_0, and at the bottom wall as θ_w. The cylinder is thermally insulated with a zero normal temperature gradient imposed on its surface. The domain is meshed using a series of macro-elements with internally applied Langrangian polynomial mapping functions. A graded element distribution is applied towards all solid boundaries to resolve regions that experience large flow gradients, such as flow separation at the cylinder corners and within the wall boundary layers/ Shercliff layers. The distribution of the macro-elements in the mesh applied in this study is shown in Fig. 2.

3.2. Validation, grid refinement, and domain dependence

In general, the SM82 model is applicable for MHD duct flows under the effect of a strong magnetic field, although some deviation from the quasi-two-dimensional behaviour can be observed in some situations of complex geometry ducts. For the case of simple rectangular duct flows, the model has been verified against the three-dimensional results [5,6], and the error using this model compared to that of the three-dimensional solution is found to be of order of 10% [8,42]. This error is significant in the vicinity of and inside the side layers. The work done by Kanaris et al. [43] demonstrated a high degree of two-dimensionalisation of cylinder wake vortices with increasing N, which also provides an excellent validation of the model for MHD wake flows. The formulation of this model can be found in literature including [9,31,32].

To validate the numerical scheme being used, the flow over a triangular cylinder with $Pr = 0.71$ for non-MHD flow at different Reynolds number and $\beta = 0.25$ were computed. Results are compared with published numerical results by De and Dalal [18] and Srikanth et al. [20] in Table 1. The results compare well with the results by De and Dalal [18], where most results differ by less than 1%. The discrepancies observed with the results by Srikanth et al. [20] may have arisen from the different in the domain size used. The present implementation of the SM82 model has previously been used and validated in a number of quasi-two-dimensional MHD wake flow studies (see Hussam et al. [9,31,32] Hussam and Sheard [33]) and more recently in Hamid et al. [42], Cassells et al. [34].

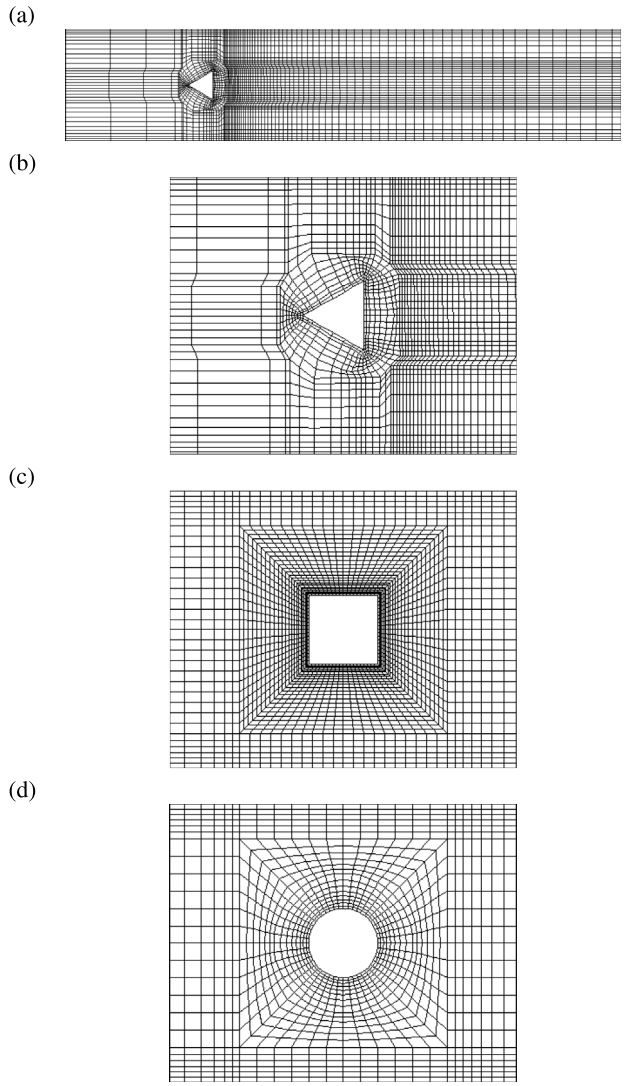

Fig. 2. (a) Macro-element distribution of the computational domain (b) Magnified mesh in the vicinity of the triangular obstacle. The full duct height is shown, while the extensive upstream and downstream duct lengths are omitted. (c)–(d) corresponding zoomed-in segments of meshes used for the square and circular cylinder duct flows.

Table 1
Comparison of results to published work for different values of Reynolds numbers in a zero-*Ha* flow. The values in the parentheses are the relative differences (%) between the results from the present study and available published data.

Re		$\overline{C_d}$	*St*	$\overline{Nu}$
80	Present study	1.6470	0.1954	4.4280
	De and Dalal [18]	1.64	0.195	4.6
		(0.43%)	(0.22%)	(0.61%)
	Srikanth et al [20].	1.6357	0.1919	4.8695
		(0.69%)	(1.84%)	(4.96%)
100	Present study	1.6829	0.2045	5.2870
	De and Dalal [18]	1.68	0.206	5.3
		(0.17%)	(0.23%)	(0.24%)
	Srikanth et al [20].	1.6708	0.2004	5.5624
		(0.72%)	(2.06%)	(4.95%)
150	Present study	1.9715	0.2258	6.8099
	De and Dalal [18]	1.96	0.225	6.8
		(0.59%)	(0.34%)	(0.15%)
	Srikanth et al [20].	1.9349	0.2212	7.1270
		(1.89%)	(2.07%)	(4.45%)

Table 2
Domain lengths defining the meshes used to test the effect of the domain lengths of the confined triangular cylinder meshes. N_{el} is the number of macro elements, and x_u and x_d describe the inlet and outlet domain sizes, respectively.

	M_1	M_2	M_3
N_{el}	3933	4050	4208
x_u	8	10	12
x_d	25	30	42

A comprehensive grid resolution study was conducted to ensure that adequate domain sizes, and spatial and temporal resolutions are maintained for the simulations described in this study. Three families of meshes were tested for $Re = 3000$ and $Ha = 2400$, being the upper bound of Reynolds and Hartmann numbers considered in this study. The upstream and downstream domain length chosen are shown in Table 2. For each domain length, elements of polynomial degree $N_p = 8$ were employed, and the flow was evolved to a saturated state. The changes in the time-averaged drag coefficient $\overline{C_d}$, the vortex shedding frequency *St*, the RMS of the lift coefficient $C_{l,\mathrm{rms}}$, the time-averaged integral of the magnitude of velocity over the computational domain $\mathcal{L}^2$ norm, and the time-averaged Nusselt number $\overline{Nu}$ were quantified. A difference of less than 1% was found when comparing values of the output parameters between the M_2 and M_3 meshes. Hence, the M_2 mesh sizing was used hereafter, which contains 4050 spectral-elements.

A spatial resolution study was conducted at the same flow parameters by gradually increasing the order of interpolation of the polynomial shape function N_p (N_p^2 nodes per macro-element) over $5 \leq N_p \leq 9$, while keeping the macro-element distribution unchanged. The time-averaged integral of the magnitude of velocity over the computational domain $\mathcal{L}^2$ norm, and the time-averaged Nusselt number $\overline{Nu}$ were monitored. The results from the saturated flow solution obtained using $N_p = 8$ achieves a precision of better than 0.5% to the flow solution obtained using $N_p = 9$, and this resolution is used hereafter. Furthermore, we conducted additional convergence analysis on the post processing methods used to obtain the Nusselt number. The data acquisition points and sampling frequency were refined to accurately estimate the time history of local Nusselt number without significant error or aliasing. A sampling frequency of 100 samples per unit time was used across the simulations.

4. Results and discussion

4.1. Transition from steady to time dependent flow

In this study, the critical Reynolds number above which the flow past the body becomes oscillatory in nature is calculated using the Stuart–Landau equation, which describes the non-linear behaviour of a perturbation about the transition [9,44,45]. Following Provansal et al. [44], the Stuart–Landau equation is written as

$$\frac{\mathrm{d}A}{\mathrm{d}t} = (\sigma + i\omega)A - l(1 + ic)\left|A^2\right|A + ..., \tag{16}$$

where A is a measure of the complex amplitude of the evolving instability as a function of time ($A = |A|\exp(i\zeta)$, $|A|$ the signal magnitude, ζ the phase of the mode, σ is the infinitesimal growth rate, l and c are coefficients describing the non-linear regime, and ω the angular frequency of the signal in the linear regime. The above equation can be decomposed into real and imaginary components as

$$\frac{\mathrm{d}(\log|A|)}{\mathrm{d}t} = (\sigma - l|A|^2) + ..., \tag{17}$$

$$\frac{\mathrm{d}\zeta}{\mathrm{d}t} = (\omega - lc|A|^2) + ... \tag{18}$$

For supercritical bifurcations ($l > 0$), the transition behaviour near

the onset of the instability can be described by the first two terms of Eq. (17). $d\log|A|/dt$ against $|A|^2$ should thus relate linearly, and the intercept value as $|A|^2 \rightarrow 0$ corresponds to the linear growth rate of the instability, and the sign of the gradient at this point determines the nonlinear evolution characteristics of the instability. Collecting σ for several Reynolds number, and extrapolating to zero growth rate yields the critical Reynolds number.

The variation of the critical Reynolds number with Hartmann numbers for the values of Hartmann number $320 \leq Ha \leq 2400$ and blockage ratio $\beta = 0.25$ is presented in Fig. 3. In order to understand the difference in the MHD flow dynamics with comparison to the square and circular cylinders under similar flow conditions and blockage ratio, the critical Reynolds number results for the triangular cylinder are compared with the numerical results of Chatterjee and Gupta [10] for the square cylinder, and Dousset and Pothérat [8] for the circular cylinder. The critical Reynolds number increases monotonically with increasing Hartmann number for all the cases. This is not surprising given that higher Hartmann numbers (i.e. a stronger magnetic field) act to weaken transverse fluctuations in the channel, resulting in a higher Reynolds number required to invoke the transition. The damping effect of the imposed magnetic field can be inferred from the momentum equation of the quasi-two-dimensional Navier–Stokes equations, Eq. (2), where the exponential growth rate of the flow instabilities is shifted by Ha/Re through the linear damping action of the Hartmann layers. However, it is found that the critical Reynolds number in the case of the triangular cylinder is much smaller than those of the circular and square cylinders. This is due to the existence of sharper corners in the case of a triangular cylinder which alters the dynamics and instabilities of the flow [46,47]. In contrast, the smooth surface in the case of the circular object renders better stability to the flow. As a result, the transition Reynolds number is higher in the case of a circular cylinder in comparison to that of the square and triangular cylinders. The percentage reduction of the relative difference between the critical Reynolds numbers for the various obstacles are found to be about 50 %− 34% for $320 \leq Ha \leq 2160$ with respect to the value of the square cylinder's critical Reynolds numbers, and about 60 %− 40% with respect to the value of the circular cylinder's critical Reynolds numbers.

The consequence of the lower critical Reynolds numbers for the triangular obstacle in comparison to those of the square and circular obstacle is that for a given Reynolds number, unsteady flow (i.e. vortex shedding) can be maintained to a significantly greater Hartmann number. For instance, at $Re = 600$, vortex shedding behind a circular cylinder is suppressed beyond $Ha = 580$, whereas it can be sustained up to $Ha = 1650$ behind a triangular obstacle.

5. Flow structures

To demonstrate the effect of the magnetic field on the interaction of the wall boundary layer parallel to the magnetic field (the Shercliff layers) with those of the cylinder (vortex shedding), The instantaneous vorticity fields for $Re = 800$ at different Hartmann numbers are illustrated in Fig. 4. At $Ha = 320$, a typical Kármán vortex street is observed. Regular vortices are shed from alternate sides of the cylinder forming two rows of vortices that rotate clockwise and counter-clockwise, respectively, along with the formation of secondary vortices entrained from the Shercliff layers. As the vortices convect downstream (approx. $x = 4d$), they interact significantly with the Shercliff layers, merging and rolling up together before traveling further downstream. For $Ha = 640$, the behaviour is similar, though the wake vortices from the upper and lower sides of the obstacle adopt a wider separation from the wake centreline, and the vortices dissipate more rapidly as they convect downstream. The vorticity entrainment from the Shercliff layers decrease significantly as the Hartmann number is increased from $Ha = 640$ to $Ha = 1160$. With a further increase in the Hartmann number to $Ha = 2400$, vortex shedding is completely suppressed and the wake is composed of two shear layers which are reflection symmetric about the duct centreplane.

5.1. Lift and drag coefficient

The temporal variation of the lift coefficient with Hartmann number for $Re = 800$ is presented in Fig. 5. The lift coefficient signal preserves a time-dependent oscillation for $Ha = 320$, 640 and 1160 which is a result of the periodic flow characteristic demonstrated in Fig. 4. Furthermore, it is observed that the amplitude of oscillation decreases gradually with increasing Hartmann number from $Ha = 320$ to 1160. For $Ha = 2400$, no oscillation in the lift signal is detected as vortex shedding is completely suppressed at that Hartmann number.

The Fourier spectrum of the lift coefficient signal for $Ha = 320$ and $Re = 800$ presented in Fig. 5 is plotted in Fig. 6. Consistent with Fig. 5, the spectrum exhibits a strong harmonic peak which reflects the uniform periodic behaviour observed in the lift coefficient time history. However, the interaction of the Kármán vortices with Shercliff layers (see Fig. 4) suggests that secondary frequencies will develop simultaneously with the primary vortex shedding frequency. To further investigate the presence of secondary frequencies in the flow, a spectral analysis of the vorticity time series signal is recorded on the duct centreline at streamwise locations four, eight, twelve, sixteen and twenty diameters downstream of the cylinder. Fig. 7 displays the vorticity time history for $Ha = 320$ and $Ha = 1160$ at $x = 4d$ and $y = 0$. The respective Fourier spectrum of the vorticity signal for $Ha = 320$ shown in Fig. 7 is presented in Fig. 8. For $Ha = 320$ at different x/d, the time-dependent vorticity (not shown) demonstrates a sequence of vortices with alternating senses of rotation with the intensity being highest at $x = 4d$. It was observed that irrespective of the position where the signal was acquired, the spectrum peak is located at the same dominant frequency. The spectra is the secondary harmonic has a power density of about 40-60% of the primary's. 'dominated' and 'significantly' sounds a bit too strong for this usage. The first peak is fairly consistent for all x/d, while the harmonics are progressively stronger at greater distances downstream. These spectra support the visualization of the flow shown in Fig. 4(a–c), where the flow is characterised by the formation of vortices shed from the cylinder along with the formation of secondary vortices that detach from the side walls.

The effect of Hartmann number on the time-averaged drag coefficient, $\overline{C_d}$, is presented in Fig. 9. Following Dousset and Pothérat [8], it is found that the drag coefficient data exhibits a collapse to a universal curve when plotted against $Re/Ha^{0.8}$, with $\overline{C_d}$ observed to first decrease to a minimum of $\overline{C_d} = 1.2$ at $Re/Ha^{0.8} = 2$, before subsequently

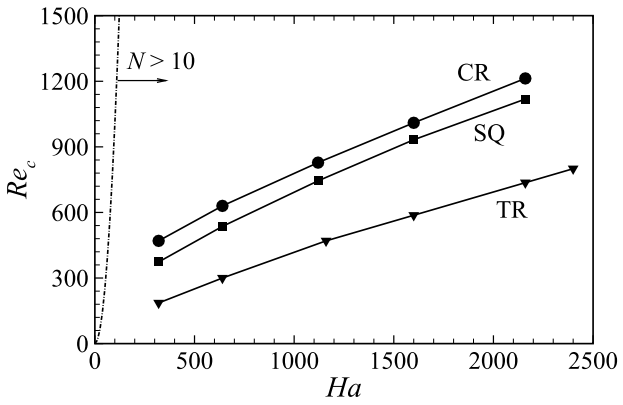

Fig. 3. Critical Reynolds number for onset of vortex shedding plotted against Ha for the three different shapes as indicated for a duct with a blockage ratio $\beta = 0.25$. The dash-dotted line is the $N = 10$ curve: the Re_c values predominantly lie to the right of that curve, demonstrating the suitability of the quasi-two-dimensional assumption as $N \gg 1$. CR, SQ and TR represents circular [8], square [10] and triangular cylinder, respectively.

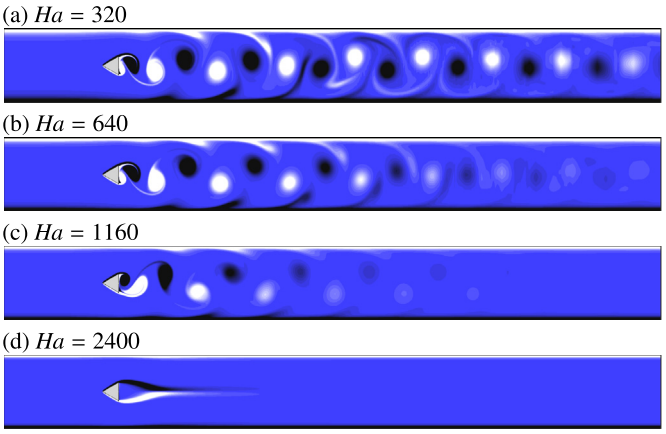

Fig. 4. Vorticity contour plots for $Re = 800$ and Hartmann number as indicated. 20 contour level are displayed between $-2 \leq \Omega \leq 2$, with light and dark contours representing positive and negative vorticity, respectively.

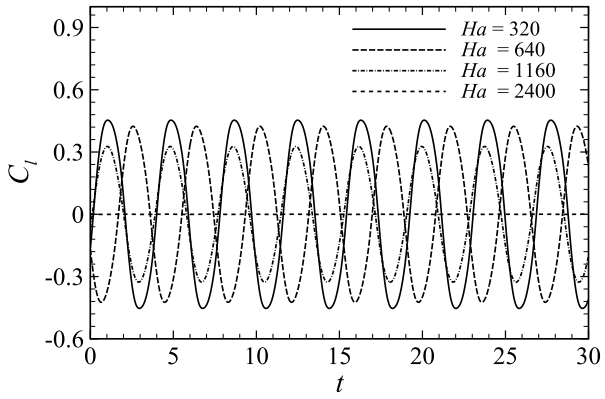

Fig. 5. Time history of the lift force coefficient C_l at different Hartmann numbers as indicated for $Re = 800$.

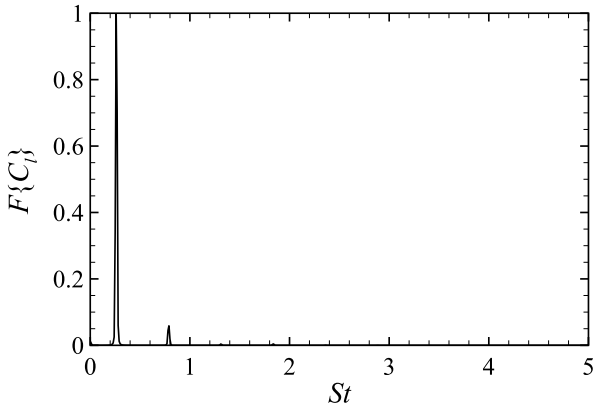

Fig. 6. Fourier spectrum of the lift coefficient ($F\{C_l\}$) for $Re = 800$ and $Ha = 320$.

increasing to a plateau of approximately $\overline{C_d} = 1.8$ at larger values of $Re/Ha^{0.8}$. Results for the circular [8,9] and square cylinder [10] demonstrated that at low values of $Re/Ha^{0.8}$, the data similarly collapses onto a universal curve. However, in contrary to the present results, those studies observed that at higher $Re/Ha^{0.8}$, the drag coefficient exhibited a dependence on the Hartmann number.

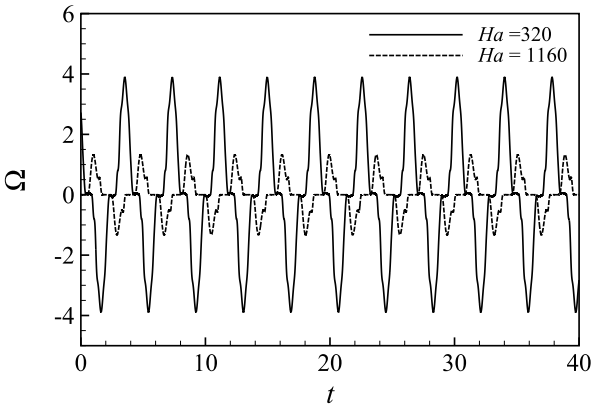

Fig. 7. Time history of the vorticity signal taken at $x/d = 4$ and $y/d = 0$ for $Re = 800$ at Hartmann number $Ha = 320$ and $Ha = 1160$.

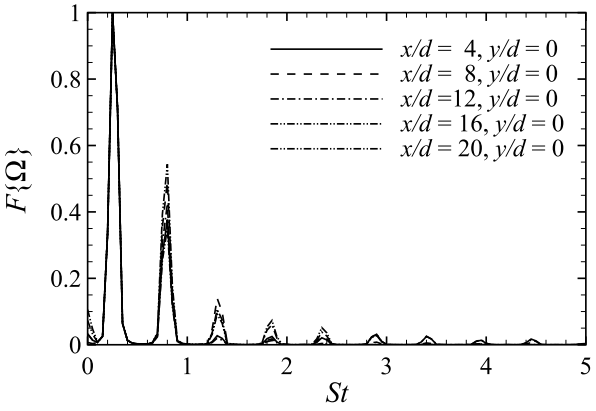

Fig. 8. Fourier spectrum of the vorticity signal ($F\{\Omega\}$) multiple streamwise positions x/d and $y/d = 0$ for $Re = 800$ and $Ha = 320$.

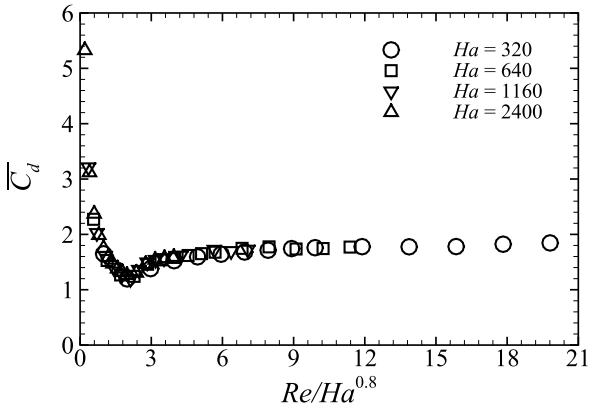

Fig. 9. Time-averaged drag coefficients as a function of $Re/Ha^{0.8}$ at different Hartmann numbers as indicated.

5.2. Heat transfer

To illustrate the effect that the magnetic field has on the wall heat transfer, instantaneous temperature contours are presented in Fig. 10 for a range of Hartmann numbers at a constant $Re = 800$. The initial observation from these contours is that, due to the strong interaction between the side wall vortices and the Kármán vortex street, the thermal field in the absence of the magnetic field (i.e. $Ha = 0$) is more irregular and chaotic than those of the MHD flows. For $Ha \leq 1160$, the temperature fields are time-dependent since the flows are unsteady the oscillatory cross-stream velocity field induced by the periodically shed

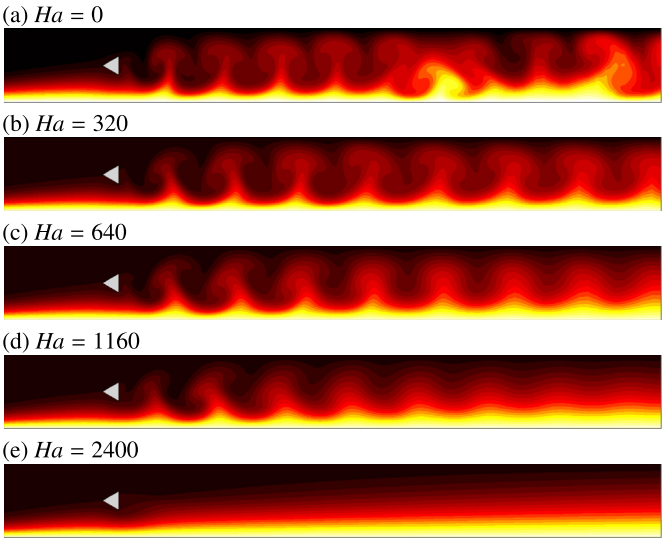

Fig. 10. Instantaneous dimensionless temperature contours at $Re = 800$ for Hartmann number as indicated. Dark and light contours correspond, respectively, to colder and hotter regions, with contours plotted over $\theta_0 \le \theta \le \theta_w$.

vortices act to perturb the thermal boundary layer. Thus, the colder fluid is transported towards the hot region of the channel and the hotter fluid near the heated wall is convected away to mix with the cooler bulk flow. This process enhances the mixing between the cold fluid and the heated surface, and as a result the heat transfer is enhanced. However, on further increasing the Hartmann number to $Ha = 2400$, reversion to steady flow eradicates the convective heat transport leading to an increase in the thickness of the thermal boundary layer. Hence, the temperature flux through the heated wall decreases. Similar observations with regards to convective heat transport in MHD flow past a circular cylinder in a duct at different blockage ratio were reported in Refs. [9] and [10] for a square cylinder at $\beta = 0.25$. Hence, the thermal transport characteristics of MHD flow in a heated channel with an obstacle of different geometries are qualitatively similar. However, the quantitative difference is expected to be significant.

Now the local Nusselt number at different Harmann numbers will be considered as a function of position along the heated duct wall. Fig. 11 presents the distribution of the time-averaged local Nusselt number $\overline{Nu}_w(x)$ along the heated wall as a function of streamwise coordinate for different Hartmann numbers at $Re = 800$. It is found that the effect of Hartmann number on the distribution of the local Nusselt number along the heated wall is substantial. A monotonic decrease in $\overline{Nu}_w(x)$ is observed for the steady-state case at $Ha = 2400$ where the heat transport is not enhanced by transverse convection invoked by the wake vortices interacting with the side walls. The Hartmann numbers producing unsteady flow exhibit higher $\overline{Nu}_w(x)$ over most of the downstream region (except close to the cylinder), and that the increase in $\overline{Nu}_w(x)$ is greater at smaller *Ha*. With decreasing *Ha*, the extent of the region on the heated duct wall downstream of the cylinder over which the local Nusselt number increases is observed to increase. The location of the maximum local Nusselt number moves downstream from nearly $x/d \approx 5$ to $x/d \approx 13.5$. This occurs because in this region there is a strong interaction between the Shercliff layer adjacent to the heated duct side-wall and the cylinder wake vortices which is reflected in the vorticity field plot shown in Fig. 4(a). However, for $Ha = 640$ and 1160, the peak local Nusselt numbers occur at a closer location downstream of the cylinder (i.e. approximately $x/d = 5$). This is due to the fact that with increasing *Ha* the wake dissipates faster and the distance downstream over which enhancement of heat transport is observed gets shorter redundant. On further increasing the Hartmann number, $\overline{Nu}_w(x)$ decreases monotonically with increasing *x*, nearly similar to the corresponding curve produced without no obstacle in the channel.

Fig. 12(a) shows the variation of the time-averaged Nusselt number $\overline{Nu}$ of the heated wall with Reynolds number for different Hartmann numbers. It can be noted that the heat transfer increases with increasing Reynolds number, while it decreases with increasing Hartmann number. At lower *Re*, the data for each Hartmann number is approximately coincident, which corresponds to the steady-state regime. The coincidence of the data may be explained by the diffusion-dominated heat transfer due to thermal conduction across the stable thermal boundary layer that is relatively insensitive to Hartmann number due to the low Prandtl number. The variation of $\overline{Nu}$ with *Re* is found to be more significant in the unsteady flow regimes compared to the steady flow regime with a noticeable difference at larger Reynolds numbers. This may be attributed to the effect of the cross-stream mixing induced by the cylinder wake near the heated wall which increases with increasing Reynolds number resulting in enhanced Nusselt numbers. For example, the increase $\overline{Nu}$ is almost 50% as Reynolds number changes from $Re = 1000$ to 2000. The dependence of the time-averaged Nusselt number on the Hartmann number is more pronounced at larger Reynolds numbers. At higher Hartmann numbers, the thermal boundary layer that develops along the heated wall becomes thicker as there is less cross-stream mixing which decreases the temperature gradient resulting in a reduction in the Nusselt number.

The percentage increment of the overall heat transfer defined by Eq. (14) for the Nusselt number data presented in Fig. 12(a) are plotted in Fig. 12(b). In order to present the comparison of the triangular cylinder heat transfer increment with those of the square and circular cylinders, the variation of heat transfer increment for those geometries are also shown in Fig. 12(b). The triangular and square cylinders are found to produce significantly greater heat transport than the circular cylinder at corresponding Reynolds and Hartmann numbers.

In order to compare the percentage increment of the overall heat transfer for each of the three geometries under the same conditions, the percentage heat transfer increment for the three different geometries for $Re = 1000$ and 2000 at $Ha = 320$ and 2400 are listed in Table 3. This demonstrates that for a moderate Hartmann number at $Re = 1000$, the square cylinder obstacle is preferable to circular and triangular cylinder, while for $Re = 2000$, the square and triangular objects behave similarly, with the triangular obstacle having approximately 6% higher $\%HI$ than the square obstacle.

This observation is attributed to the fact that for the square cylinder at $Ha = 320$ and $Re = 1000$, the vorticity and temperature contours shown in Fig. 13(c,d) reveal that there is substantial interaction between wake vortices and the heated wall due to the broadening of the width of the wake. The boundary layer entrainment from the heated wall into the wake, as well as the mixing of the hotter fluid near the heated region with the cooler core flow are stronger in the wake of the square cylinder than those for the triangular cylinder (Fig. 13a,b). This

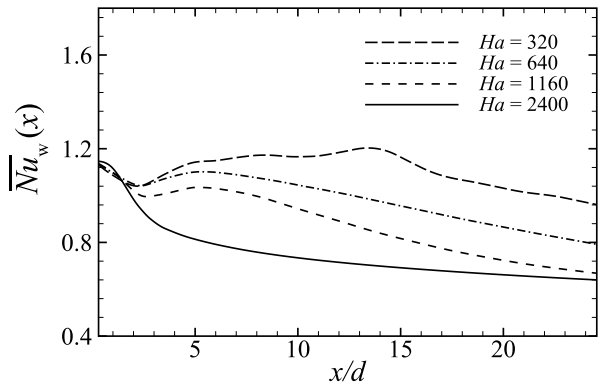

Fig. 11. Time-averaged local Nusselt number plotted against streamwise wall position along the downstream of the heated wall for $Re = 800$ and Hartmann number as indicated.

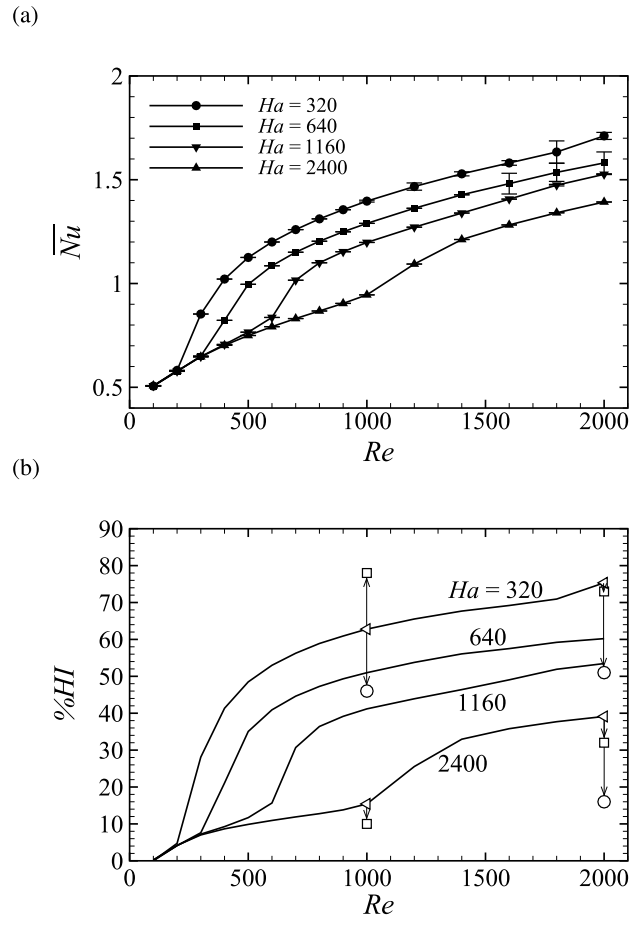

Fig. 12. (a) Variation of the time-averaged Nusselt number with Reynolds number for different Hartmann numbers as indicated. The error bars provide an uncertainty estimate in the thermal response due to the time interval used to capture the low frequency temporal variations. (b) The percentage increase in heat transfer obtained by adding triangular cylinder to the channel (%HI) as a function of Reynolds number for different Hartmann numbers as indicated. For comparison, the percentage increase in heat transfer at $Ha = 320$ and 2400, $Re = 1000$ and 2000, and $\beta = 0.25$ correspondingly generated by using a square or circular cylinder are indicated by hollow square and circular symbols, respectively. They are connected by arrows to the triangular cylinder data at the same parameters.

Table 3
Comparison of the overall heat transfer increment *%HI* for the cases with triangular, square, and circular cylinders placed in a channel of $\beta = 0.25$ at $Re = 1000$ and at $Ha = 320$ and 2400. The combinations producing the highest heat transfer increment are highlighted in bold.

%HI				
	$Ha = 320$		$Ha = 2400$	
Re	1000	2000	1000	2000
circular	46%	52%	− 1.2%	16%
square	**78%**	73%	10%	33%
triangular	62%	**75%**	**16%**	**40%**

leads to an increase in the local Nusselt number over a region extending from $x/d \simeq 5 - 15$, as shown in Fig. 14(a). For$Re = 2000$ at $Ha = 320$ as shown in Fig. 14(b), the local Nusselt number for the square cylinder exhibits a wavy pattern due to the complex interaction between the wake vortices and the thermal boundary layer of the heated wall. However, at a high Hartmann number, the triangular promoter performs better than the others. Inspection of vorticity contours for both

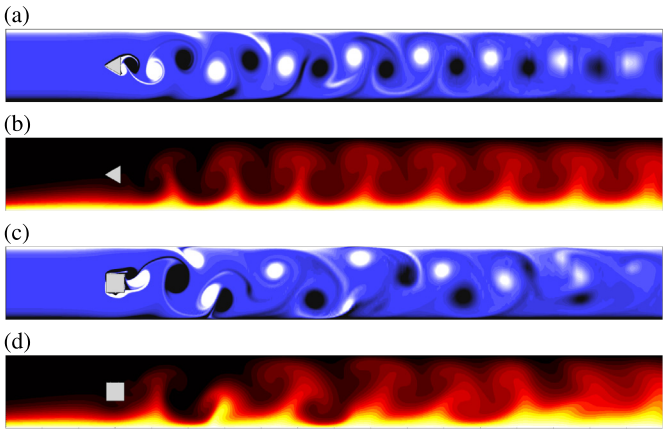

Fig. 13. Instantaneous vorticity (a,c) and temperature contours (b,d) for $Re = 1000$ and $Ha = 320$. Figures (a,b) correspond to the triangular cylinder case, and (c,d) to the square cylinder. Vorticity and temperature contours levels are as per Figs. 4 and 10, respectively.

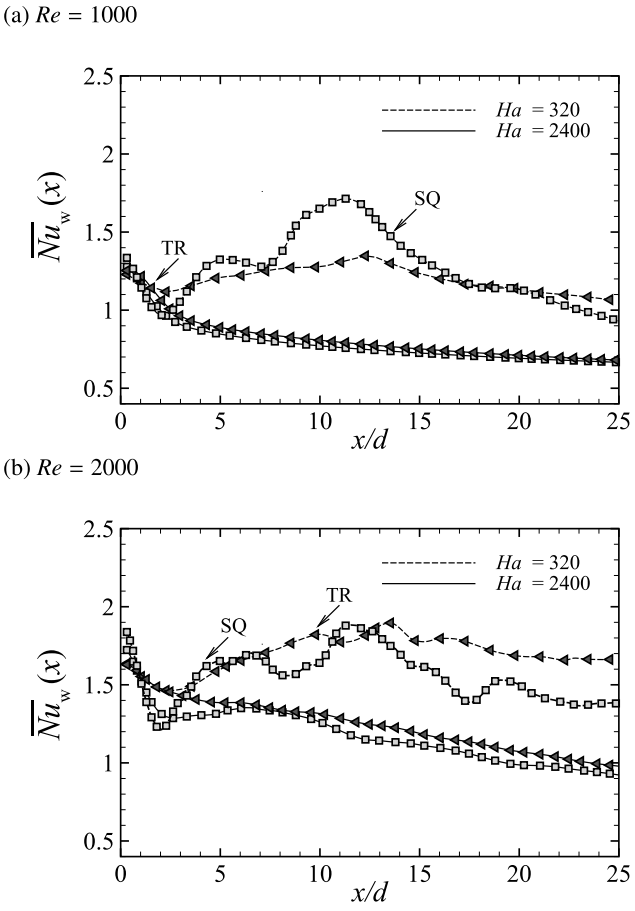

Fig. 14. Comparison of the time-averaged local Nusselt number along the heated wall, downstream of the vortex promoter (a) $Re = 1000$ and (b) $Re = 2000$ at different Hartmann numbers as indicated. Here, the labels SQ and TR correspond to the responses of the square and triangular cylinders, respectively, with marker symbols that also correspond to the cylinder geometry. Symbols are skipped in order to make the lines more visible.

TR and SQ promoters (as shown in Fig. 15) reveal an apparent difference in the strength and the dynamics of the resulting wake vortices. The shear layers emanating from the triangular cylinder almost immediately roll up and shed, while for the square cylinder, the vortices shed at a distance further downstream and diffuses rapidly as they

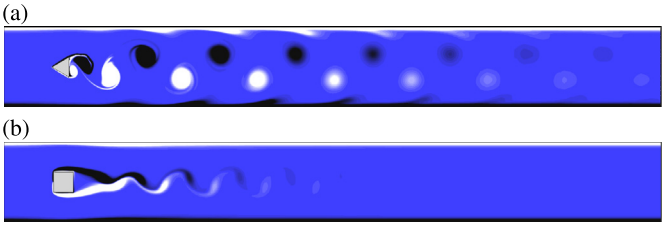

Fig. 15. Vorticity contour plots for $Re = 2000$ and $Ha = 2400$. 20 contour level are displayed between $-1 \leq \Omega \leq 1$, with light and dark contours representing negative and positive vorticity, respectively.

convect away. The peak vorticity obtained for TR at $x/d \approx 5$ is approximately four times stronger than the one for SQ at the same downstream distance, which results in a stronger wake-boundary layer interaction for TR than SQ, and thus results in a better heat transfer performance.

The general observation arising from Fig. 12(a,b) is that as *Ha* increases, the improvement in Nusselt number is seen at higher Reynolds number (due to the delay in the onset of unsteady flow), and when unsteady flow develops, the Nusselt number increase is progressively smaller with increasing *Ha*. Projecting to higher *Ha* (e.g. fusion-relevant conditions) suggests that physical vortex promoters may be of only modest usefulness in the quest for enhancement of heat transfer. Hamid et al. [35,48] demonstrated that electrically generated vortices in addition to a physical obstacle can achieve significantly greater enhancement than the physical obstacle alone. Their results showed that the enhancement in heat transfer due to the imposed current exhibits a non-monotonic relation with *Ha*. At low *Ha*, due to the competition between inertial and Hartmann damping, heat transfer enhancement increases with increasing *Ha* and then decreases steadily with further increase in *Ha*. However, in the high-*Ha* regime, Hartmann damping dominates over the driving force. As a result, a strong wake-boundary layer occurs only in the wake region. On further increasing in *Ha*, the flow becomes dominated by the forcing current only and the heat transfer eventually becomes asymptotically independent of *Ha*.

5.3. Net power balance

The inclusion of a vortex promoter within the channel supplies thermal enhancement but at the cost of the increased pressure losses. To characterise whether the enhancement of heat transfer power invoked by placing a vortex promoter within a duct exceeds the added power required due to the increased pressure loss in the duct, the net power enhancement is provided. Consistent with the analysis in Ref. [34], the enhancement in heat power due to the inclusion of the vortex promoter is

$$\Delta P_{\text{heat}} = P_{\text{heat}} - P_{0,\text{heat}}, \tag{19}$$

where P_{heat} is the heat power transferred through the heated wall, while the subscript 0 denotes the corresponding flow without cylinder. The corresponding increase in pumping power to overcome the addition of the vortex promoter is

$$\Delta P_{\text{flow}} = P_{\text{flow}} - P_{0,\text{flow}}, \tag{20}$$

where P_{flow} is the pumping power required to drive the flow through the duct. Hence, we have a net improvement if $\Delta P_{\text{heat}} > \Delta P_{\text{flow}}$ (i.e. $\Delta P_{\text{heat}}/\Delta P_{\text{flow}} > 1$). The net power balance can then be expressed as

$$\Delta P_{\text{net}} = \Delta P_{\text{heat}} - \Delta P_{\text{flow}}. \tag{21}$$

Normalizing power by $\rho d^2 U^3$ and applying the scaling outlined in Section 2 for length, velocity, pressure and temperature, the dimensionless heat and pumping power may be expressed as

$$P_{\text{heat}} = \frac{a\kappa_T C_p \delta\theta}{d^2 U^3} \int_0^{L_{\text{duct}}} \frac{\partial\theta}{\partial y} \mathrm{d}x \tag{22}$$

and

$$P_{\text{flow}} = 4\frac{a}{d} U_{\text{avg}} \Delta p, \tag{23}$$

where κ_T is the thermal diffusivity, C_p is the constant pressure specific heat capacity and U_{avg} is the area-averaged velocity through the duct inlet, which is estimated through the averaging of Eq. (15) as

$$U_{\text{avg}} = \frac{1}{4\beta h} \int_{-2}^{2} u(y) \mathrm{d}y, \tag{24}$$

$$= \frac{1}{4\beta h} \left[\frac{\sinh(4\beta\sqrt{H}) - 4\beta\sqrt{H}\cosh(\sqrt{H})}{\beta\sqrt{H}(1-\cosh(\sqrt{H})} \right]. \tag{25}$$

The net power balance is thus

$$\Delta P_{\text{net}} = \frac{a\kappa_T C_p \delta\theta}{d^2 U^3} \int_{L_{\text{duct}}} \left(\frac{\partial\theta}{\partial y} - \frac{\partial\theta_0}{\partial y} \right) \mathrm{d}x - 4\frac{a}{d} U_{\text{avg}} (\Delta p - \Delta p_0). \tag{26}$$

Normalizing the net power by the pumping power, and using $Pr = 0.022$, $C_p = 188\ \text{Jkg}^{-1}\text{K}^{-1}$, $\delta\theta = 250\text{K}$ and $U = 0.015\ \text{ms}^{-1}$, which are relevant to the fusion blanket application [39,49], the normalised net power may be expressed as

$$\frac{\Delta P_{\text{net}}}{P_{\text{flow}}} = \frac{\kappa_T C_p \delta\theta}{4dU^3 U_{\text{avg}} \Delta P} \int_0^{L_{\text{duct}}} \left(\frac{\partial\theta}{\partial y} - \frac{\partial\theta_0}{\partial y} \right) \mathrm{d}x - \left(1 - \frac{\Delta p_0}{\Delta p} \right). \tag{27}$$

The pre-factor to the heat flux integral in Eq. (27) can be rewritten in terms of dimensionless parameters as

$$\frac{\kappa_T C_p \delta\theta}{4dU^3} = \frac{1}{Pr} \frac{\nu C_p \delta\theta}{4dU^3} = \frac{1}{4PrRe} \frac{C_p \delta\theta}{U^2} = \frac{1}{4PrReEc}, \tag{28}$$

where Ec is the Eckert number $Ec = U^2/C_p\delta\theta$, which relates the kinetic energy and enthalpy in the flow.

$$\frac{\Delta P_{\text{net}}}{P_{\text{flow}}} = \frac{2.37 \times 10^9}{U_{\text{avg}} \Delta PRe} \int_{L_{\text{duct}}} \left(\frac{\partial\theta}{\partial y} - \frac{\partial\theta_0}{\partial y} \right) \mathrm{d}x - \left(1 - \frac{\Delta p_0}{\Delta p} \right). \tag{29}$$

Its clear from the form of the pre-factor that a net benefit in heat transfer will be more significant for smaller Prandtl numbers (compatible with liquid metals), smaller Reynolds number (the Reynolds numbers are relatively modest in magnetic confinement fusion blankets), and smaller Eckert number. Furthermore, the value of Eckert number tends to be of order $O(10^{-9})$, suggesting that enthalpy in the flow is substantially higher than its kinetic energy. Thus, the pre-factor is very large. This strongly amplifies the benefit of heat transfer enhancement in comparison to the required pumping power.

Fig. 16 demonstrates the variation of $\Delta P_{\text{net}}/P_{\text{flow}}$ with Reynolds

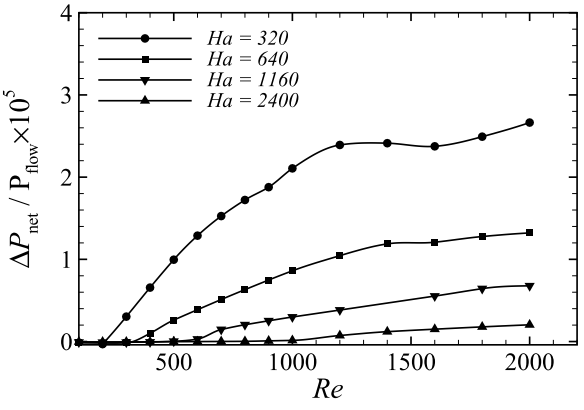

Fig. 16. Variation of normalised net power with Reynolds number for different Hartmann number as indicated.

number for different Hartmann numbers at relevant operating conditions for fusion blanket application [39,49], calculated using eqn. (29). It can be noted from the figure that $\Delta P_{net}/P_{flow}$ decreases with increasing Hartmann number. This is due to the fact that a stronger magnetic field dictates the opposing Lorentz force to be greater, which generally results in lower heat transfer characteristics and higher pressure losses. For fusion-relevant conditions across the parameter ranges considered in the present study, $\Delta P_{net}/P_{flow}$ ranges between 1.05×10^2 and 2.66×10^5, indicating a significant benefit in the rate of heat transfer over the additional pumping power required.

6. Conclusion

The characteristics of MHD flow and heat transfer in a plane channel with a built-in triangular cylinder subjected to a strong magnetic field aligned with the cylinder axis is numerically simulated using a quasi-two-dimensional model. Simulations have been performed over the range of Reynolds numbers up to 3000, $0 \leqslant Ha \leqslant 2400$ and with a constant blockage ratio $\beta = 1/4$. The results for heat transfer enhancement were compared against the square and circular cylinders to elucidate further the relationship between the gain in the heat transfer using obstacles of different geometric shapes.

The magnetic field was observed to significantly alter the structure of the wakes behind the cylinder, whereby the boundary layer detachment from the side walls was observed to decrease with increasing Hartmann number. It was found that the heat transfer enhancement was significantly associated with the resulting wake and their interactions with the heated wall. Comparisons between different shapes of promoters revealed that the CR promoter performed worst in terms of heat transfer enhancement regardless of flow conditions. The results also demonstrate that for relatively low Reynolds number and Hartmann number, SQ gives considerably better results in terms of heat transfer enhancement compared to the TR, while for higher Reynolds number, the SQ and TR cylinders act almost the same. However, for high Hartmann number, the TR promoter performs better than the SQ and CR. This is due to the fact that for high Hartmann numbers, unlike the TR, a strong wake-boundary layer occurs only in the wake region for SQ and the vortices diffuse rapidly as they convect downstream constituting a thermal resistance against the heat transfer from the heated wall to the main flow. Therefore, TR performed better than SQ and CR for fusion relevant conditions. The heat transfer enhancement exhibits similar characteristics to the hydrodynamics counterpart, whereby the local Nusselt number distribution is closely associated with the strength of the interaction between the wake boundary layer and that of the heated wall. However, with increasing Reynolds number, the average Nusselt number is found to be higher for TR than that of SQ.

Acknowledgments

This research was supported by the Australian Research Council through Discovery Grant DP150102920, high-performance computing time allocations from the National Computational Infrastructure which is supported by the Australian Government, and the Monash SunGRID. A.H.A.H. is supported by the Malaysia Ministry of Education and Universiti Teknologi MARA, Malaysia. Z.Y.N. is supported by a Faculty of Engineering International Postgraduate Research Scholarship (FEIPRS) from the Faculty of Engineering, Monash University.

References

[1] S. Münevver, Magnetohydrodynamic flow in a rectangular duct, Int. J. Numer. Meth. Fluid. 7 (7) (1987) 697–718.
[2] S. Khan, J.N. Davidson, Magnetohydrodynamic coolant flows in fusion reactor blankets, Ann. Nucl. Energy 6 (9) (1979) 499–509.
[3] R.J. Moreau, Magnetohydrodynamics, ISBN 0792309375 Kluwer Academic Publishers, Dordrecht; Boston, 1990.
[4] J. Sommeria, R. Moreau, Why, how, and when, MHD turbulence becomes two-dimensional, J. Fluid Mech. 118 (1982) 507–518.
[5] A. Pothérat, J. Sommeria, R. Moreau, An effective two-dimensional model for MHD flows with transverse magnetic field, J. Fluid Mech. 424 (2000) 75–100.
[6] A. Pothérat, J. Sommeria, R. Moreau, Numerical simulations of an effective two-dimensional model for flows with a transverse magnetic field, J. Fluid Mech. 534 (2005) 115–143.
[7] B. Muck, C. Gunther, U. Muller, L. Buhler, Three-dimensional MHD flows in rectangular ducts with internal obstacles, J. Fluid Mech. 418 (2000) 265–295.
[8] V. Dousset, A. Pothérat, Numerical simulations of a cylinder wake under a strong axial magnetic field, Phys. Fluids (1) (2008) 20 017104.
[9] W.K. Hussam, M.C. Thompson, G.J. Sheard, Dynamics and heat transfer in a quasi-two-dimensional MHD flow past a circular cylinder in a duct at high Hartmann number, Int. J. Heat Mass Tran. 54 (5) (2011) 1091–1100.
[10] D. Chatterjee, S.K. Gupta, MHD flow and heat transfer behind a square cylinder in a duct under strong axial magnetic field, Int. J. Heat Mass Tran. 88 (2015) 1–13.
[11] Z.Y. Ng, T. Vo, W.K. Hussam, G.J. Sheard, Two-dimensional wake dynamics behind cylinders with triangular cross-section under incidence angle variation, J. Fluid Struct. 63 (2016) 302–324.
[12] C.P. Jackson, A finite-element study of the onset of vortex shedding in flow past variously shaped bodies, J. Fluid Mech. 182 (1987) 23–45.
[13] B.J.A. Zielinska, J.E. Wesfreid, On the spatial structure of global modes in wake flow, Phys. Fluids 7 (6) (1995) 1418–1424.
[14] J.E. Wesfreid, S. Goujon-Durand, B.J.A. Zielinska, Global mode behavior of the streamwise velocity in wakes, J. Phys. II 6 (10) (1996) 1343–1357.
[15] A.K. De, A. Dalal, Numerical simulation of unconfined flow past a triangular cylinder, Int. J. Numer. Meth. Fluid. 52 (7) (2006) 801–821.
[16] A. Dalal, V. Eswaran, G. Biswas, A finite-volume method for Navier-Stokes equations on unstructured meshes 54 (3) (2008) 238–259.
[17] H. Chattopadhyay, Augmentation of heat transfer in a channel using a triangular prism, Int. J. Therm. Sci. 46 (5) (2007) 501–505.
[18] A.K. De, A. Dalal, Numerical study of laminar forced convection fluid flow and heat transfer from a triangular cylinder placed in a channel, J. Heat Tran. 129 (5) (2007) 646–656.
[19] H. Abbassi, S. Turki, S.B. Nasrallah, Numerical investigation of forced convection in a plane channel with a built-in triangular prism, Int. J. Therm. Sci. 40 (7) (2001) 649–658.
[20] S. Srikanth, A. Dhiman, S. Bijjam, Confined flow and heat transfer across a triangular cylinder in a channel, Int. J. Therm. Sci. 49 (11) (2010) 2191–2200.
[21] H. Abbassi, S. Turki, S.B. Nasrallah, Mixed convection in a plane channel with a built-in triangular prism, Numer. Heat Tran. Part a: Applications 39 (3) (2001) 307–320.
[22] H. Abbassi, S. Turki, S.B. Nasrallah, Channel flow past bluff-body: outlet boundary condition, vortex shedding and effects of buoyancy, Comput. Mech. 28 (1) (2002) 10–16.
[23] M. Bouhalleb, H. Abbassi, Pressure drop and heat transfer enhancement in a plane channel with a built-in bluff body: a comparison between triangular prism and square cylinder, Prog. Comput. Fluid Dynam. Int. J. 14 (5) (2014) 295–303.
[24] L.G. Kit, Y.B. Kolesnikov, A.B. Tsinober, P.G. Shtern, Use of a conduction anemometer in investigating the MHD wake behind a body, Magnetohydrodynamics 5 (1969) 46–50.
[25] L. Kit, S. Turntaev, A.B. Tsinober, Investigation with a conducting anemometer of the effect of magnetic field on disturbances in the wake of a cylinder, Magnetohydrodynamics 6 (3) (1970) 331–335.
[26] Y.B. Kolesnikov, A.B. Tsinober, Two-dimensional turbulent flow in a channel with inhomogeneous electrical conductivity of the walls, Magnetohydrodynamics 8 (3) (1972) 23–31.
[27] O.V. Andreev, Y. Kolesnikov, MHD instabilities at transverse flow around a circular cylinder in an axial magnetic field, in: A. Alemany, P. Marty, J.P. Thibault (Eds.), Transfer Phenomena in Magnetohydrodynamic and Electroconducting Flows: Selected Papers of the PAMIR Conference Held in Aussois, France, 22-26 September, 1997; Vol. 51 of Fluid Mechanics and its Applications, Kluwer Academic Publishers, Aussois, France, 1997, pp. 205–210 ISBN: 978-3-642-03085-7.
[28] O.V. Andreev, Y. Kolesnikov, Experimental flow around a conducting cylinder in an axial homogeneous magnetic field, Magnetohydrodynamics 34 (1997) 286–293.
[29] M. Frank, L. Barleon, U. Müller, Visual analysis of two-dimensional magnetohydrodynamics, Phys. Fluids 13 (8) (2001) 2287–2295.
[30] K. Ueno, K. Saito, S. Kamiyama, Three-dimensional simulation of mhd flow with turbulence, JSME Intl J Series B 44 (1) (2001) 38–44.
[31] W.K. Hussam, M.C. Thompson, G.J. Sheard, Optimal transient disturbances behind a circular cylinder in a quasi-two-dimensional magnetohydrodynamic duct flow, Phys. Fluids (2) (2012) 24 024150.
[32] W.K. Hussam, M.C. Thompson, G.J. Sheard, Enhancing heat transfer in a high Hartmann number magnetohydrodynamic channel flow via torsional oscillation of a cylindrical obstacle, Phys. Fluids 24 (11) (2012) 113601.
[33] W.K. Hussam, G.J. Sheard, Heat transfer in a high Hartmann number MHD duct flow with a circular cylinder placed near the heated side-wall, Int. J. Heat Mass Tran. 67 (2013) 944–954.
[34] O.G.W. Cassells, W.K. Hussam, G.J. Sheard, Heat transfer enhancement using rectangular vortex promoters in confined quasi-two-dimensional magnetohydrodynamic flows, Int. J. Heat Mass Tran. 93 (2016) 186–199.
[35] A.H.A. Hamid, W.K. Hussam, G.J. Sheard, Combining an obstacle and electrically driven vortices to enhance heat transfer in a quasi-two-dimensional MHD duct flow, J. Fluid Mech. 792 (2016) 364–396.
[36] L. Barleon, U. Burr, K. Mack, R. Stieglitz, Magnetohydrodynamic heat transfer research related to the design of fusion blankets, Fusion Technol. 39 (2001) 127–156.
[37] A. Pothérat, Quasi-two-dimensional perturbations in duct flows under transverse

magnetic field, Phys. Fluids (2007) 19 074104.
[38] U. Burr, L. Barleon, U. Müller, A. Tsinober, Turbulent transport of momentum and heat in magnetohydrodynamic rectangular duct flow with strong sidewall jets, J. Fluid Mech. 406 (2000) 247–279.
[39] B. Schulz, Thermophysical properties of the li (17) pb (83) alloy, Fusion Eng. Des. 14 (3) (1991) 199–205.
[40] S. Smolentsev, C. Wong, S. Malang, M. Dagher, M. Abdou, MHD considerations for the DCLL inboard blanket and access ducts, Fusion Eng. Des. 85 (2010) 1007–1011.
[41] G.E. Karniadakis, M. Israeli, S.A. Orszag, High-order splitting methods for the incompressible Navier–Stokes equations, J. Comput. Phys. 97 (2) (1991) 414–443.
[42] A.H.A. Hamid, W.K. Hussam, A. Pothérat, G.J. Sheard, Spatial evolution of a quasi-two-dimensional Kármán vortex street subjected to a strong uniform magnetic field, Phys. Fluids (2015) 27 053602.
[43] N. Kanaris, X. Albets, D. Grigoriadis, S. Kassinos, Three-dimensional numerical simulations of magnetohydrodynamic flow around a confined circular cylinder under low, moderate, and strong magnetic fields, Phys. Fluids (7) (2013) 25 074102.
[44] M. Provansal, C. Mathis, L. Boyer, Bénard-von Kármán instability: transient and forced regimes, J. Fluid Mech. 182 (1987) 1–22.
[45] G.J. Sheard, M.C. Thompson, K. Hourigan, A coupled Landau model describing the Strouhal–Reynolds number profile of a three-dimensional circular cylinder wake, Phys. Fluids 15 (2003) L68–L71.
[46] G.J. Sheard, M.J. Fitzgerald, K. Ryan, Cylinders with square cross-section: wake instabilities with incidence angle variation, J. Fluid Mech. 630 (2009) 43–69.
[47] S. Luo, X. Tong, B.C. Khoo, Transition phenomena in the wake of a square cylinder, J. Fluid Mech. 23 (2) (2007) 227–248.
[48] A.H.A. Hamid, W.K. Hussam, G.J. Sheard, Heat transfer augmentation of a quasi-two-dimensional MHD duct flow via electrically driven vortices, Numer. Heat Tran. Part A-applications 70 (2016) 847–869.
[49] S. Smolentsev, R. Miraghaie, M. Abdou, MHD effects on heat transfer in a molten salt blanket, Fusion Sci. Technol. 47 (3) (2005) 559–563.